Comparison of fan-beam, slit-slat and multi-pinhole collimators for molecul breast tomosynthesis

van Roosmalen, Jarno; Beekman, Freek; Goorden, Marlies

DOI
10.1088/1361-6560/aabfa3

Publication date
2018

Document Version
Final published version

Published in
Medical Physics

PAPER

Comparison of fan beam, slit-slat and multi-pinhole collimators for molecular breast tomosynthesis

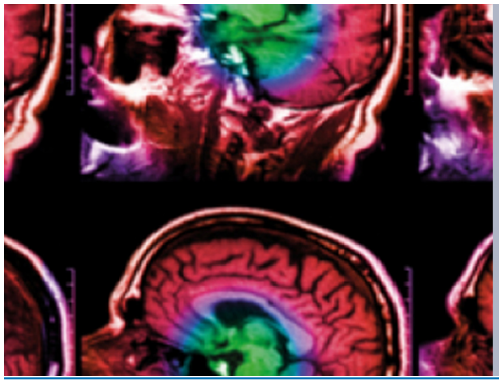

IOP Publishing Phys. Med. Biol. 63 (2018) 105009 (12pp) https://doi.org/10.1088/1361-6560/aabfa3

Physics in Medicine & Biology

IPEM Institute of Physics and Engineering in Medicine

PAPER

Comparison of fan beam, slit-slat and multi-pinhole collimators for molecular breast tomosynthesis

RECEIVED
5 November 2017

REVISED
17 April 2018

ACCEPTED FOR PUBLICATION
20 April 2018

PUBLISHED
16 May 2018

Jarno van Roosmalen[1], Freek J Beekman[1,2] and Marlies C Goorden[1]

[1] Section Radiation, Detection and Medical Imaging, Delft University of Technology, Delft, Netherlands
[2] MILabs B.V., Utrecht, Netherlands

E-mail: jvroosmalen@gmail.com

Keywords: molecular imaging, breast, fan beam, slit-slat, pinhole

Abstract

Recently, we proposed and optimized dedicated multi-pinhole molecular breast tomosynthesis (MBT) that images a lightly compressed breast. As MBT may also be performed with other types of collimators, the aim of this paper is to optimize MBT with fan beam and slit-slat collimators and to compare its performance to that of multi-pinhole MBT to arrive at a truly optimized design. Using analytical expressions, we first optimized fan beam and slit-slat collimator parameters to reach maximum sensitivity at a series of given system resolutions. Additionally, we performed full system simulations of a breast phantom containing several tumours for the optimized designs. We found that at equal system resolution the maximum achievable sensitivity increases from pinhole to slit-slat to fan beam collimation with fan beam and slit-slat MBT having on average a 48% and 20% higher sensitivity than multi-pinhole MBT. Furthermore, by inspecting simulated images and applying a tumour-to-background contrast-to-noise (TB-CNR) analysis, we found that slit-slat collimators underperform with respect to the other collimator types. The fan beam collimators obtained a similar TB-CNR as the pinhole collimators, but the optimum was reached at different system resolutions. For fan beam collimators, a 6–8 mm system resolution was optimal in terms of TB-CNR, while with pinhole collimation highest TB-CNR was reached in the 7–10 mm range.

1. Introduction

Several molecular imaging systems dedicated to breast imaging have recently emerged that can detect sub-centimetre lesions with high sensitivities (Abreu *et al* 2006, Brem *et al* 2008, Hruska and O'Connor 2008, Raymond *et al* 2008, Luo *et al* 2010). Clinical studies have already shown that molecular breast imaging may play a role as supplemental screening modality in addition to mammography (Rhodes *et al* 2015, Brem *et al* 2016, Shermis *et al* 2016) and in monitoring the response to chemotherapy (Mankoff *et al* 2002, Mitchell *et al* 2013). Hruska and O'Connor (2013) and Fowler (2014) provide comprehensive overviews of molecular breast imaging modalities and Hruska (2016) gives an outlook into current and future developments.

In our group, we are investigating and optimizing a scanner to perform 3D imaging of single-gamma emitting tracer distributions in the breast (van Roosmalen *et al* 2016, 2017). We showed that the proposed molecular breast tomosynthesis (MBT) scanner equipped with multi-pinhole collimators could significantly improve tumour-to-background contrast-to-noise ratios (TB-CNR) over those of planar systems that also image mildly compressed breasts (van Roosmalen *et al* 2016). We subsequently optimized sensitivity of multi-pinhole geometries for a range of fixed system resolutions (van Roosmalen *et al* 2018). We found that the geometries with system resolutions in the 7.0 mm–10.0 mm range gave best results in terms of TB-CNR for small lesions (4.0–6.0 mm) in a breast shaped phantom. Moreover, the simulations showed no significant differences for the scanner's performance when it was equipped with either a continuous NaI(Tl) based detector or a pixelated CZT detector.

Although the use of pinholes in MBT gave promising results, pinhole collimation is not the only option available. For situations in which the imaging field-of-view (FOV) is smaller than the detector size-which is the case for MBT-a converging collimator geometry such as a fan beam or cone beam is also often used (Moore *et al* 1992, Formiconi *et al* 2004, Weinmann *et al* 2009, Capote *et al* 2013). Compared to parallel-hole collimation, converging

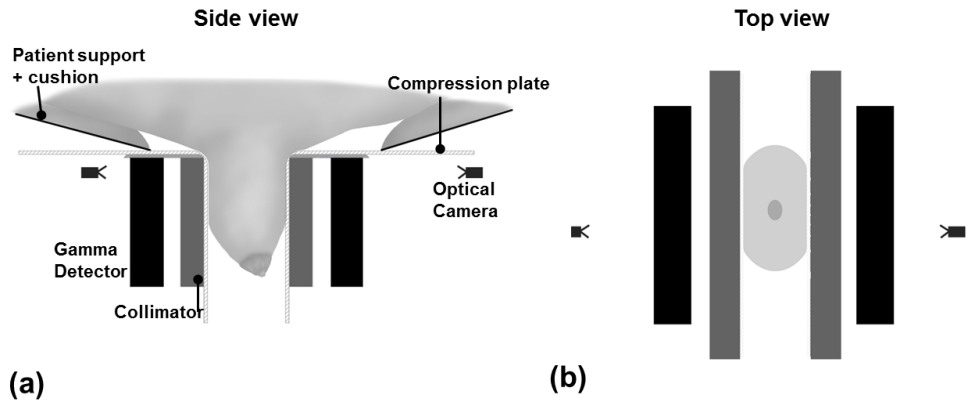

Figure 1. Schematic illustration of the geometry of the MBT scanner including compression plates, collimators, and gamma detectors. (a) Side view showing breast of a woman lying prone on the scanner table. The breast is placed in the opening in the bed and slightly compressed. (b) Top view of the breast between the transparent compression plates (artist impression). Note that details on collimator geometry are not shown here as we will investigate different types of collimators in this work.

collimators can improve the sensitivity by utilizing the whole detector surface. Moreover, the slanting of the holes allows for the object to be seen from multiple angles which is necessary if one wants to extract 3D information. For MBT, the appropriate converging collimator would be a fan beam collimator, as in the anterior direction the detector is not larger than the largest breast the scanner should accommodate. A second type of collimator that may be of interest for MBT is the slit-slat collimator as it combines properties of both pinhole and fan beam or parallel hole collimators (Daekwang and Metzler 2012).

The aim of this paper is to compare performance of multi-pinhole, fan beam and slit-slat collimation for MBT. To this end, we first analytically optimize sensitivity of fan beam and slit-slat collimators at a range of fixed system resolution (5–11 mm). We subsequently compare the performance of these optimized geometries in full system simulations with the earlier optimized multi-pinhole designs.

2. Methods

In this section, we describe the basic design of MBT, the optimization process and how we evaluate the results. In general, we follow the same methodology as in our earlier pinhole optimization study (van Roosmalen *et al* 2018) in which more details can be found.

2.1. Molecular breast tomosynthesis (MBT)

In the recently proposed MBT scanner (Beekman 2014, van Roosmalen *et al* 2016), the patient lies prone on a specially designed bed with the mildly compressed breast pendant through a hole and with the scanner underneath as schematically shown in figure 1. In our initial MBT design, two Tungsten plates served as collimators each containing 63 pinholes in a focused arrangement. The focused design gives the MBT scanner the unique ability to scan a user-defined volume-of-interest (VOI), which is beneficial as it increases the count yield from the VOI (Beekman *et al* 2005, van der Have *et al* 2009). To image any volume, the FOV has to be translated over the breast such that the desired scan volume is viewed over a range of angles (Vastenhouw and Beekman 2007, Vaissier *et al* 2012). In MBT this FOV translation is done by synchronized step-and-shoot movement of the collimators and detectors in a plane parallel to the compression plates, i.e. the collimators and detector are translated along both the anterior-posterior and the left–right axes to form a grid of scanning positions. During iterative image reconstruction, all available projection data from all positions is used to reconstruct the 3D MBT image (Vastenhouw and Beekman 2007).

2.2. Previous pinhole optimization

In a recent work, we optimized sensitivity of multi-pinhole designs for a range of fixed system resolutions and compared simulated images of a tumour-containing digital breast phantom for these optimized designs (van Roosmalen *et al* 2018). We found that the geometries with system resolution in the range of 7.0 mm–10.0 mm gave optimal results in terms of TB-CNR. This was true both for MBT with conventional gamma detectors based on a continuous NaI(Tl) scintillator read out by PMTs (3.2 mm intrinsic resolution) and pixelated detectors (1.6 mm pixels), with no significant differences between them. Therefore, in this work we only evaluate MBT using continuous NaI(Tl) detectors, as these are much more cost effective than pixelated detectors. In the results section of this work we present results from the previous pinhole optimization study in order to compare multi-pinhole with fan beam and slit-slat collimation.

Table 1. List of parameters for fan beam collimated geometries.

Parameter	Description	Value	Varied/fixed
L	(mm) Detector-breast distance		Free
L_h	(mm) Length of holes		$L - s_{FB}$
D_x, D_z	(mm) Dimensions of the detector	250, 150	Fixed
F_x	(mm) Focal distance in coronal plane, from collimator surface	40	Fixed to enable focused scanning
R_i	(mm) Intrinsic spatial resolution of detector	3.2	Fixed
R_t	(mm) Targeted system resolution	5, 6, 7, 8, 9, 10, 11	We optimize at several fixed values
t	(mm) Septal thickness	>=0.3	Minimum imposed, further determined by Gunter's penetration criterium
d_x, d_y	(mm) Hole diameter		Calculated to keep system resolution constant
s_{FB}	(mm) Distance breast to collimator face	4	Fixed at minimal feasible value

2.3. System design for fan beam and slit-slat collimators

We restrict the collimator-detector geometries in our optimization such that they fit into the previously presented MBT concept in which a lightly compressed breast is imaged with two focusing collimators that each project onto a gamma detector.

2.3.1. General considerations for collimator design

For both fan beam and slit-slat collimation, we restrict ourselves by the following design principles:

1. Due to the light compression of the breast used in MBT, we account for a minimal distance of 4 mm between the breast and the collimator face to accommodate the 4 mm thick compression plates.
2. We assume a conventional gamma camera based on a NaI(Tl) scintillator and PMT readout (3.2 mm intrinsic resolution) with fixed detector size of 250 × 150 mm.
3. We compare focused collimator designs that enable scanning of VOIs smaller than the whole breast as targeted imaging allows increasing the local count yield. We control the amount of focusing such that the FOV is comparable to that of the earlier pinhole collimators. Below we explain for each collimator type how this is achieved.
4. The septal thickness must be sufficiently large to prevent septa penetration by the 140 keV gamma photons as emitted by ^{99m}Tc. For this, we use the rule provided by Gunter (1996). To make sure that the collimators are manufacturable we impose a minimum septal thickness of 0.3 mm.

2.3.2. Fan beam specific considerations for collimator design

In the anterior direction, the detector is not much larger than the average breast (110 mm, see section 2.6.1), and smaller than the size of the largest breasts (at least up to 200 mm (Scopinaro *et al* 1999)). Therefore, we do not focus in the sagittal plane but only in the coronal plane, which means that we use a fan beam collimator rather than a cone beam geometry. A fan beam collimator can be fully characterised by a small set of parameters, listed in table 1 and depicted in figure 2. We control the amount of focusing by fixing the focal length F_x of the fan beam collimators to the value of 40 mm. This makes the FOV comparable to that of the optimized pinhole collimators in van Roosmalen *et al* (2018).

2.3.3. Slit-Slat specific considerations for collimator design

The parameters for slit-slat collimators are listed in table 2 and illustrated in figure 3. The plate containing the slits is made of 6 mm thick tungsten, which provides sufficient stopping power for 140 keV photons letting through a fraction of 1.5×10^{-9}. The slats cover the whole space between the plate with slits and the detector. The slits are placed in the coronal plane, in exactly the same focusing arrangement as the pinholes in van Roosmalen *et al* (2018) meaning that they are directed such that (i) they focus on a line 40 mm from the collimator (see figure 3) and (ii) they result in non-overlapping tiled projections. Generally, increasing the opening angle α of the slits will allow for less slits to be used (because of the requirement of non-overlapping projections) but will also lead to a larger volume sensitivity per slit as the FOV for each slit becomes larger. Initial simulations showed that these effects largely cancel out meaning that the choice of α does not have a large influence on the resolution-sensitivity trade-off. Therefore, α of all slits is set to the same value such that the central slit's projection is 25 mm wide, which results in a constant number of 7 slits for all configurations. This is similar as done in the pinhole optimization study (van Roosmalen *et al* 2018).

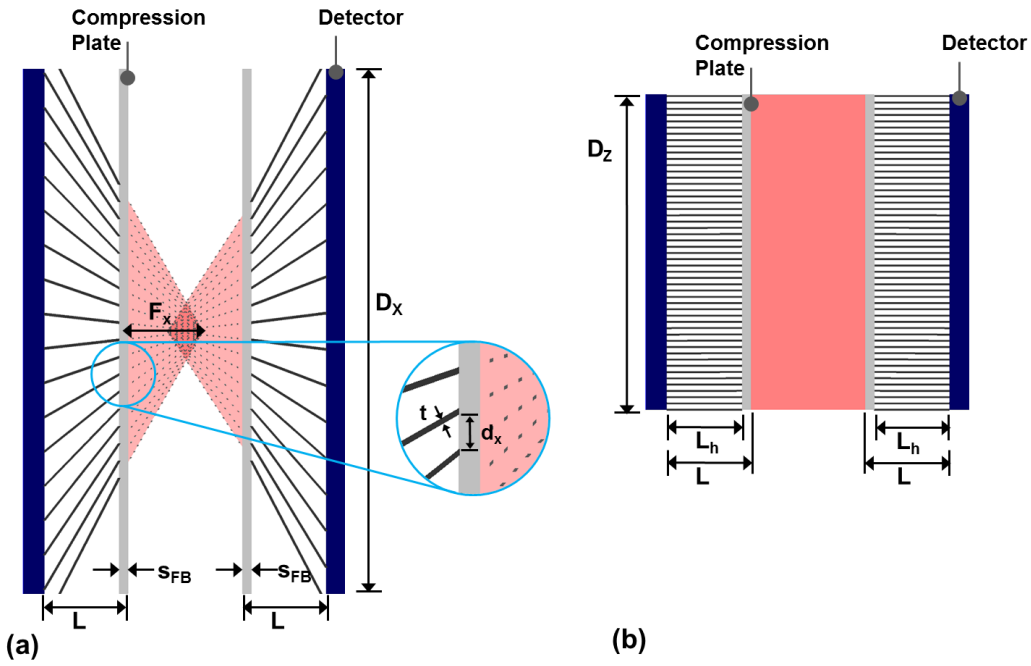

Figure 2. Example of a fan beam configuration. Two views are shown: (a) a coronal plane cross section and (b) a sagittal plane cross section. The detector, FOV, transparent compression plates and the collimators are indicated with blue, red, light grey, and dark grey respectively. Different parameters used are shown in the figure.

Table 2. List of parameters for slit-slat collimated geometries.

Parameter	Description	Value	Varied/fixed
L	(mm) Detector-breast distance		Free
D_x, D_z	(mm) Dimensions of the detector	250, 150	Fixed
F_x	(mm) Focal distance in coronal plane, from collimator surface	40	Fixed to enable focused scanning
R_i	(mm) Intrinsic spatial resolution of detector	3.2	Fixed
R_t	(mm) Targeted system resolution	5, 6, 7, 8, 9, 10, 11	We optimize for several values
T	(mm) Septa thickness	>=0.3	Minimum imposed, further determined by Gunter's penetration criterium
d_y	(mm) Hole diameter		Calculated to keep system resolution constant
W	(mm) Slit width		Calculated to keep system resolution constant
A	Slit opening angle		Calculated to keep size of central projection 25 mm, same value set for all slits
s_{ss}	(mm) Distance breast to slit centre	6	Fixed at minimal feasible value

For every change in the geometry, e.g. a different L, the slits should be repositioned to fully cover the detector with non-overlapping projections. For this, an automatic placement script was used in a similar way as for pinhole geometries. This was described in detail in van Roosmalen *et al* (2018).

2.4. Analysis of different collimators based on sensitivity-resolution trade-off

We start the analysis of different geometries with an analytical optimization in which the sensitivity is maximized at fixed system resolution. We choose a range of different target system resolutions ranging from 5 to 11 mm. This range was chosen to encompass the optimal range of 7–10 mm found earlier for pinhole collimation. For each system resolution the fan beam and slit-slat designs with the highest sensitivity were selected and further analysed with full system simulations. After analysing these full system simulations, we assured that the optimal system was within the chosen resolution range.

We report sensitivity averaged over the breast shaped region described in section 2.6.1. In our design in which the detector and collimator are translated over a sequence of positions, sensitivity depends on the sequence chosen, which is provided in section 2.5. A sensitivity-weighted averaged resolution is determined over the same region, and the hole diameters, inter-slat distance and/or slit width are iteratively adjusted until the desired target

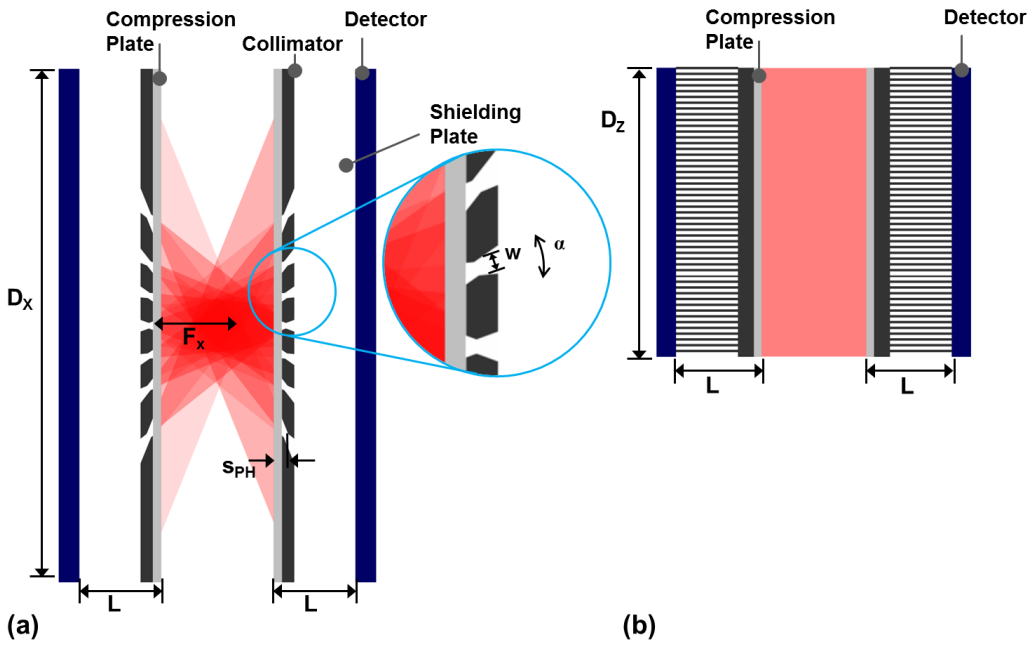

Figure 3. Example of a slit-slat beam configuration. Two views are shown: (a) a coronal plane cross section and (b) a sagittal plane cross section. The detector, FOV, transparent compression plates and the collimators are indicated with blue, red, light grey, and dark grey respectively. Different parameters used are shown in the figure.

system resolution is reached. The initial dimensions for this process are found by inverting the appropriate analytical resolution formula given below for the centre voxel.

2.4.1. *Fan beam specific analysis*

Sensitivity formulas traditionally used for converging collimators diverge near the focus (Formiconi 1998) and as we focus within the breast these cannot be used. We therefore use a recently derived expression to determine sensitivity (van Roosmalen and Goorden 2017) which we do not reproduce here due to its length.

The resolution for a fan beam collimator is different in the vertical and horizontal direction and for each direction given by Moyer (1974)

$$R_{FB} = \sqrt{\frac{R_i^2 (F - z_0)^2}{(F + L_e)^2} + d^2 \frac{(z_0 + L_e)^2}{Le^2} \frac{\left(F + \frac{L_e}{2}\right)^2}{(F + L_e)^2} \frac{1}{\cos^2 \theta_{FB}}} \tag{1}$$

where F is the focal distance for this collimator dimension, which in our case is F_x in the coronal plane and infinite in the other direction, z_0 is the distance from the collimator face, diameter d is either d_x or d_z depending on the direction and θ_{FB} is the angle between the collimator axis and the line from the focus to the position where resolution is to be determined. The effective collimator length $L_e = L_h - 2/\mu$ incorporates the effect of septal penetration via linear attenuation coefficient μ of the collimator material which is 3.39 mm^{-1} for Tungsten which is the material assumed for all MBT collimators.

2.4.2. *Slit-slat specific analysis*

For sensitivity appropriate expressions have been derived in Accorsi *et al* (2008). The authors recommend using different approximations in different parts of the FOV, and we calculated sensitivity this way. As this involves several lengthy expressions we do not reproduce the sensitivity equations here. As for resolution, in the coronal plane the same formula as for pinhole resolution is to be used which reads

$$R_{PH} = \sqrt{w_e^2 \left(1 + \frac{1}{M}\right)^2 + \left(\frac{R_i}{M}\right)^2}, \tag{2}$$

where M is the magnification factor of the slit (i.e. the ratio between distance from source to slit, and slit to detector), and w_e the effective slit-width given by Accorsi *et al* (2008) as

$$w_e = w + \frac{\ln 2}{\mu} \left(\tan^2 \frac{\alpha}{2} - \cot^2 \theta_{ss}\right) \cot \frac{\alpha}{2} \sin \phi_0. \tag{3}$$

Here θ_{ss} is the angle between the plane of the slit and the line from slit to source, and ϕ_0 the incidence angle from the source through the centre of the slit onto the detector.

In the sagittal plane, the resolution is governed by the slats and can be calculated using the converging collimator expression as given in (1) with an infinite focal length (which is just the common parallel hole resolution formula).

2.5. Sampling and scan positions

As mentioned above, the scan volume of MBT can be selected by the user and the collimator-detector pairs are then moved over a sequence of positions in a plane parallel to the compression plates in order to scan the VOI. In principle, the scan sequence should be adjusted to the size of the breast that is scanned and the shape of the FOV which is different for both types of collimators. However, as we compare a large number of designs and need to be sure we compare them equally we use a single set of sequences for all designs for both collimator types. In the sagittal plane, both collimators apply slats (see figures 2 and 3). In regions close to the collimator where the surface of the breast is located, the sensitivity just in front of the septa will be strongly reduced compared to that in front of the holes. Therefore, we move the collimator and detector 1 mm in the anterior direction for a second position so that every position is in front of the holes at least once. Furthermore, in the posterior position the collimators and detectors are moved from left to right in 4 mm steps from −76 to 76 mm while in the anterior position, the left to right steps are 8 mm from −74 to 74 mm. The bigger step size in the anterior position is to keep the number of bed positions low. Note that the positions in the anterior position are staggered compared to those in the posterior position; this improves the uniformity of the sampling. Note that by moving the collimator over the breast, angular coverage in the coronal plane is increased to a maximal full angle coverage that can be approximated by $2\tan^{-1}\frac{D_x/2}{F_x+L}$ (see figures 2 and 3). We will provide this angle for all simulated designs.

2.6. Validation by simulations of breast phantom scans

In the full system simulations we performed after the analytical optimization, we employed the same ray-tracing simulator (Wang *et al* 2017) both to generate simulated projections as well as a system matrix for image reconstruction. As its input, the simulator uses the collimator modelled as a voxelized volume, with a voxel size of 1/24th mm. The depth-of-interaction in the scintillator, collimator penetration, detector efficiency and detector resolution are modelled. We assumed detector pixels of 1.072 mm in a 234 × 140-pixel grid.

Phantom projections (phantom voxel size 0.5 mm) were obtained with the raytracer cut off set at 1% (Wang *et al* 2017). A uniform attenuation coefficient in the phantom of 0.0151 mm^{-1} valid for 140 keV photons in water was assumed. Phantom projections for each of the scan sequence positions were obtained, accounting for the scan time and adding Poisson distributed noise to each projection. We already showed that in our geometry torso scatter hardly affects images (Wang *et al* 2017) and it is therefore not modelled in this paper.

Images were reconstructed on a 1.0 mm isotropic voxel grid using maximum likelihood expectation maximization (MLEM) (Shepp and Vardi 1982) using a system matrix with 1.0 mm source voxel grid and a threshold of 2%. The discrepancy in grid size between phantom and reconstruction, and between cut off thresholds is to mimic a continuous activity distribution without any actual cut off. Moreover, no attenuation correction was applied.

2.6.1. *Breast phantom*

In this paper, we use the same phantom as in our earlier work (van Roosmalen *et al* 2016, 2017) which models the breast as half an elliptically shaped disk (Dong *et al* 2011), with a 110 mm chest-to-nipple distance, a width of 150 mm, and a thickness of 55 mm. The phantom is placed such that the top of the activity is at the same place as the start of the useful field of view of the detector. We placed four sets with three lesions each in the phantom (6.0, 5.0, 4.5, 4.0 mm diameter), see figure 5(a). Within each set the central lesion was placed at a depth of 22 mm, with the other two lesions at a depth of 33 mm. We assumed a background activity concentration of 3.7 kBq ml^{-1}, consistent with an injection of 925 MBq ^{99m}Tc-Sestamibi (Hruska *et al* 2012, Mann *et al* 2012) and a concentration of 37 kBq ml^{-1} in the lesions to give a tumour-background uptake ratio of 10:1 (Maublant *et al* 1996, Lee *et al* 2004, Hruska and O'Connor 2008, Sullivan *et al* 2012). We set a scan time of 10 min.

2.6.2. *Analysis of images*

Besides visually inspecting different images, we compared different breast phantom images by calculating the TB-CNR, given by

$$TB\text{-}CNR = \frac{\overline{S} - \overline{B}}{\sigma_B}. \quad (4)$$

Here $\overline{S}$ is the average signal taken in a spherical region placed on top of the lesion, $\overline{B}$ is the average signal in a background region, and σ_B is the standard deviation in the background region and serves as measure of the noise.

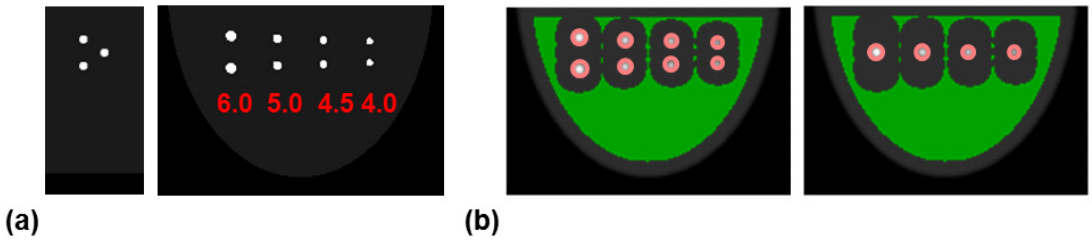

Figure 4. Slices through the breast phantom (a) left: slice parallel to sagittal plane through the 6.0 mm lesions, right: transverse slice at depth of two lesions. Lesion sizes indicated. (b). Transverse slices with red circles indicate the regions-of-interest used to determine the tumour signal while the green area denotes the background region.

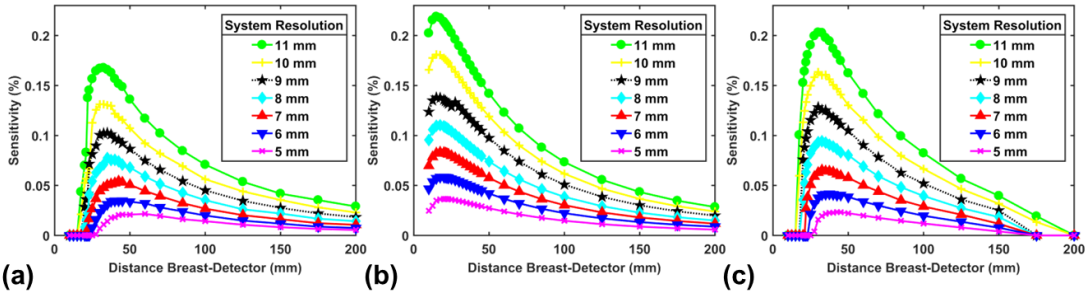

Figure 5. Sensitivity (averaged over the breast) for (a) pinhole, (b) fan beam, (c) slit-slat collimators as function of distance between detector and breast with the lines indicating different fixed system resolutions (5, 6, 7, 8, 9, 10, and 11 mm).

The regions used are indicated in figure 4(b). All simulations are repeated for 20 different noise realizations, and the average of the TB-CNR values is reported.

3. Results

3.1. Analytical optimization

After considering the design restrictions, both collimator types have only one free parameter left: the distance between the breast and the detector. All the other parameters are fixed, used to control resolution, or directly related to other parameters. For a range of system resolutions, the sensitivity as function of the distance between breast and detector is plotted in figure 5. This figure shows the fan beam and slit-slat collimators optimized in this work as well as results for the pinhole collimators from the previous study (van Roosmalen *et al* 2018). For all collimator types an optimal distance exists which depends on the system resolution. For slit-slat collimation we find optimal detector-breast distances varying between 30.0 and 42.5 mm similar to the range found for pinholes which was in between 32.5 and 60 mm, while for fan beam collimation these distances are smaller and are between 15 and 21 mm. Two opposing effects play a role; placing the detector closer by increases the solid angle covered which is beneficial for the sensitivity, while on the other hand the magnification decreases meaning that the hole sizes have to decrease to maintain resolution which in turn reduces the sensitivity. The sharp drop in sensitivity for all collimator types when moving very close to the breast comes at the point that it becomes impossible to achieve the given fixed system resolution with that type of collimator. Apparently fan beam collimators can still achieve the target resolution at closer distances than pinhole or slit-slat collimators. The maximum achievable sensitivity as function of the system resolution is shown in figure 6. This figure shows that both fan beam and slit slat collimators can achieve a higher sensitivity than the pinhole collimators at the same fixed system resolution, with the fan beam collimator having the highest sensitivity. At 5.0 mm system resolution, the optimal sensitivity of the slit-slat system is 8% higher than that of the pinhole systems, while the fan beam system has a 69% higher sensitivity. At 11.0 mm system resolution, the differences are 21% and 31% respectively. For comparison we show the resolution and sensitivity of the most sensitive parallel hole collimator from a highly optimized planar molecular breast imaging system (Hruska *et al* 2012). This system has much higher sensitivity than the other systems at equal system resolution, but of course it does not provide 3D information (see discussion section).

3.2. Full system simulations

Full system simulations were performed for each of the optimal configurations (maximum in figure 5, and geometries summarized in tables 3–5). The images depend on the number of iterations of MLEM used and the FWHM of the 3D Gaussian post-filter applied. We determined an optimal combination of iteration number

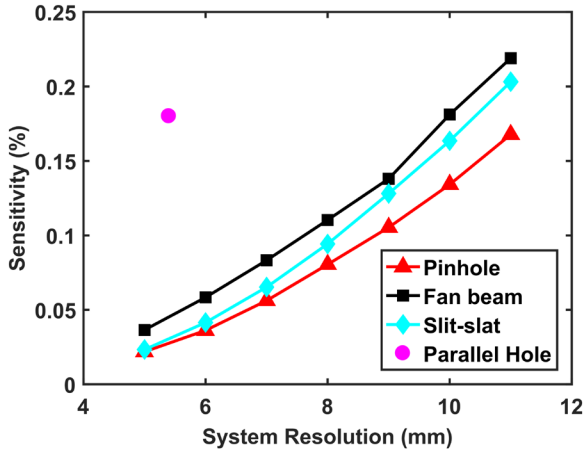

Figure 6. Plot of maximum reachable sensitivity as function of system resolution for pinhole, fan beam, and slit-slat collimators. For each system resolution, the detector-breast distance that gives the highest sensitivity at that fixed resolution is used (maximum in figure 5). For comparison a point (pink) is added showing an optimized parallel hole system from Hruska *et al* (2012).

and filter level in the following way: Gaussian filters with FWHM ranging from 0 to 8 mm (in 1 mm steps) were applied to all images and the iteration number and filter combination that lead to the highest TB-CNR in the 6.0 mm lesions (on average over the noise realizations) was determined, requiring at least 5 iterations to ensure a minimum level of convergence. These optimal number of iterations and filter level and the resulting TB-CNR are listed in tables 3–5. The tables also list the noise (the standard deviation divided by the mean over all voxels) near the chest wall (top 5 mm of reconstructed images). For all collimators, this noise level reduces when sensitivity increases. For the majority of fixed system resolutions, the pinhole collimators lead to most noise near the chest wall, while fan beam and slit-slat have lower and comparable numbers. For example, for a fixed 6.0 mm system resolution the pinhole system has a 48% and 69% higher chest wall noise level than the fan beam and slit-slat systems respectively. For the 10.0 mm system resolution this difference reduces to 7% and 0% respectively.

Slices through reconstructed images are shown in figure 7. From this figure, one can infer that in the saggital plane, the lesions are better recovered, i.e. more spherical, for the fan beam collimators than for the pinhole and slit-slat collimators which show more elongation. One possible explanation is that as the optimal fan beam collimators have the detector closer by, the angular sampling range (indicated in tables 3–5 and discussed in section 2.5) may be larger resulting in better through-plane resolution.

In figure 8, TB-CNR curves are shown as function of system resolution. From this figure one can infer that the slit-slat collimators do not reach the same TB-CNR as the other two collimator types. The reconstructed images in figure 7 also indicate that slit-slat collimation provides a lower contrast than the other collimators. Furthermore, we see that the TB-CNR results of the pinhole and fan beam collimators are close for the largest lesions. For the 6.0 mm lesions, we concluded in our earlier work that the pinhole collimator optimum is reached for the 7–10 mm system resolution geometries with the absolute peak at a TB-CNR of 10.7 for a fixed 8 mm system resolution. Fan beam collimators perform very similar, but with a small peak at 6 mm system resolution with a TB-CNR value of 10.6. For the smaller lesions, we find that the higher resolution systems are more favourable. For the 5.0 mm lesions pinhole collimation leads to an optimal TB-CNR of 5.1 at 8.0 mm system resolution while the fan beam has an optimum of 5.4 at 6.0 mm system resolution, compared to a TB-CNR of 4.7 at 6.0 mm for the slit-slat collimator. For all simulations, we note that the spread between the noise realizations is large, with a trend to reduce for lower system resolutions.

4. Discussion

In this paper, we optimized focusing fan beam and slit-slat configurations in order to find the geometry that achieves the highest sensitivity at fixed system resolutions. We simulated the optimal systems and performed a TB-CNR analysis to evaluate the spatial resolution-sensitivity trade-off. The TB-CNR ratio is linked to detectability via the Rose-criterion (Currie 1968, Rose 1973, Cherry *et al* 2012) and a relevant indicator for the possibility to use quantification to find regions with increased uptake. Moreover, TB-CNR does not require a large number of noise realizations and can quickly be calculated for many systems, iterations and filter levels. Therefore, we were able to compare the TB-CNR for optimized geometries with different fixed system resolutions.

In figure 6, we also showed the resolution and sensitivity of a parallel hole collimator for a highly optimized planar molecular breast imaging system (Hruska *et al* 2012). Note that such a parallel hole geometry only provides 2D information while the geometries considered in this paper result in 3D reconstructed images.

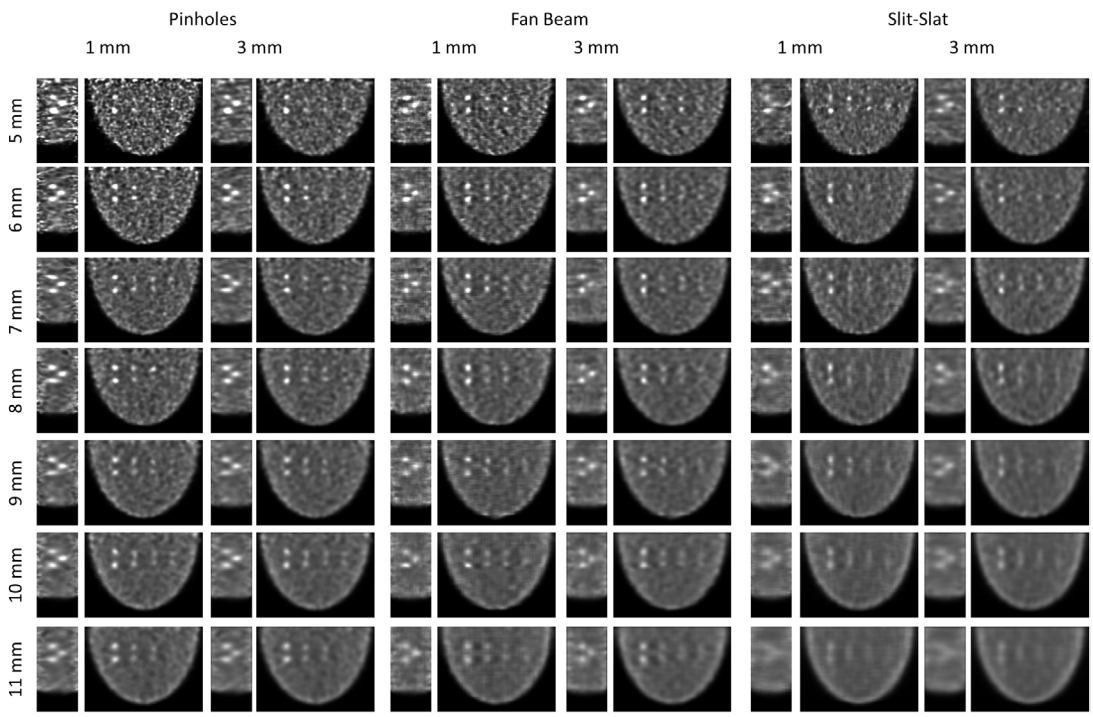

Figure 7. Simulated images of a breast shaped phantom containing lesions of 4.0, 4.5, 5.0 and 6.0 mm Alternating images show sagittal slices through the lesions, and transverse slices at the depth of two lesions. Each row represents a different target system resolution, while the different columns represent the different collimator types (pinhole, fan beam and slit-slat) and show two different filter levels (1.0 and 3.0 mm FWHM Gaussian filter). The number of iterations for each system is listed in tables 3–5.

Resolution in such reconstructed images can be higher than calculated system resolution. The same planar parallel hole geometry was simulated in an earlier comparison of MBT with planar molecular breast imaging (van Roosmalen *et al* 2016). In that study, we showed that an MBT system with a 6 mm system resolution obtained a 110% higher TB-CNR for 6.0 mm lesions than the planar imaging system despite the better sensitivity-system resolution trade off of the latter.

It is notable that two different collimator types (multi-pinhole and fan beam) show a very similar performance in terms of TB-CNR all though sensitivity (at fixed system resolution) was higher for the fan beam collimator at the same system resolution (typically by 48%). This similarity in TB-CNR is reached although the geometries of both collimators are clearly different; the pinhole collimators have a few holes accepting photons from many angles, while the fan beam collimators have many holes accepting photons from a small cone. Furthermore, the slit-slat collimators, which perform better than multi-pinhole collimators in terms of sensitivity-resolution trade-offs (on average slit-slat has 20% higher sensitivity), do worse on reconstructed images. This shows that collimator optimization is a complicated process and that the performance of a collimator depends on multiple factors such as resolution, sensitivity, size of the FOV and angular sampling over that FOV and that full system simulations are necessary for evaluation of different designs.

Scatter in the torso and in the breast can affect the images obtained with any breast imaging modality. For the simulations in this study we did not model scatter, a decision based on earlier findings from Wang *et al* (2017) in which we considered multi-pinhole MBT. In this previous paper, the reconstruction matrix was always obtained with a voxelized raytracer (as is done in this paper), but projections were either simulated with raytracing or with full Monte Carlo simulations (that included both scatter from the breast and scatter from the torso). We found that the images based on projections obtained with Monte Carlo simulations and corrected for scatter with the commonly used Triple Energy Window scatter correction method were very close to those obtained with raytracing. Combined with the superior speed of the voxelized raytracer, we therefore decided to use raytracing for the current study and did not model scatter. In future research it is of interest to also investigate the influence of scatter on reconstructed images for a fan beam or slit-slat collimator geometry.

Note that to obtain similar images from an experimental MBT system as those simulated in this paper, system calibration is required to obtain accurate system matrices. These can e.g. be based on point source measurements like used for existing preclinical multi-pinhole SPECT (van der Have *et al* 2008).

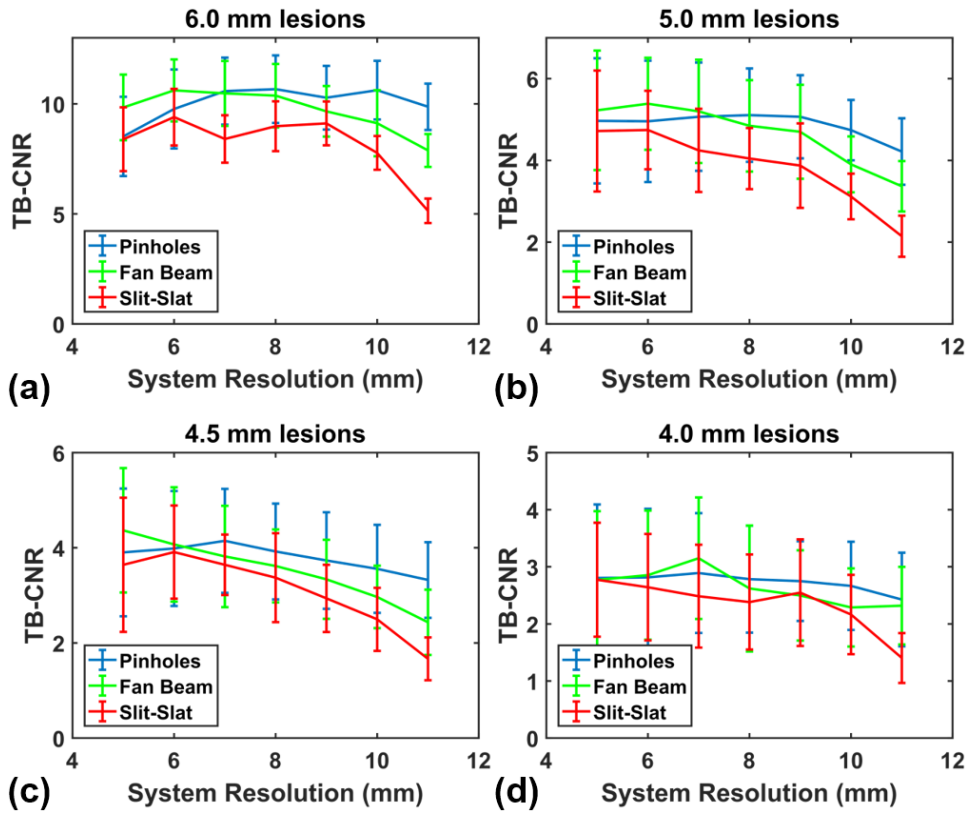

Figure 8. Plot of the TB-CNR as function of system resolution, where the TB-CNR is obtained as the maximum over iterations 5–32 and Gaussian filters with 0–10 mm FWHM as indicated in tables 3–5. The different lines represent the different collimator types and results are shown for (a) 6.0 mm lesions, (b) 5.0 mm lesions, (c) 4.5 mm lesions and (d) 4.0 mm lesions.

Table 3. Pinhole configurations.

System resolution (mm)	5.0	6.0	7.0	8.0	9.0	10.0	11.0
Detector-breast distance (mm)	60	45	42.5	35	35	32.5	32.5
Pinhole diameters (mm)	2.48	2.44	2.95	2.98	3.46	3.68	4.13
Angular range (degrees)	103	112	113	118	118	120	120
Volumetric sensitivity over whole breast (%)	0.022	0.035	0.054	0.077	0.103	0.131	0.168
Sensitivity in focus (%)	0.087	0.130	0.191	0.259	0.346	0.424	0.520
Optimal iteration	11	14	16	17	17	19	20
Optimal filter FWHM (mm)	5	4	4	3	2	1	1
Optimal TB-CNR	8.5	9.8	10.6	10.7	10.3	10.6	9.9
Standard deviation near chest wall (<5mm)	0.49	0.47	0.37	0.37	0.34	0.29	0.28

Table 4. Fan beam configurations.

System resolution (mm)	5.0	6.0	7.0	8.0	9.0	10.0	11.0
Detector-breast distance (mm)	21	20	17.5	17.5	15	15	15
Hole diameters (mm) horizontal/vertical	1.68/1.11	1.86/1.36	1.82/1.43	2.03/1.64	1.85/1.55	2.09/1.77	2.27/1.95
Septa thickness (mm)	0.30/0.30	0.30/0.30	0.30/0.30	0.30/0.30	0.32/0.30	0.36/0.30	0.39/0.30
Angular range (degrees)	128	129	131	131	133	133	133
Volumetric sensitivity over whole breast (%)	0.037	0.058	0.083	0.110	0.138	0.181	0.219
Sensitivity in focus (%)	0.167	0.273	0.397	0.539	0.684	0.839	1.002
Optimal iteration	16	17	19	22	22	22	25
Optimal filter FWHM (mm)	4	3	3	2	2	2	2
Optimal TB-CNR	9.8	10.6	10.5	10.4	9.7	9.1	8.0
Standard deviation near chest wall (<5mm)	0.33	0.33	0.32	0.30	0.29	0.27	0.28

Table 5. Slit slat configurations.

System resolution (mm)	5.0	6.0	7.0	8.0	9.0	10.0	11.0
Detector-breast distance (mm)	42.5	37.5	32.5	32.5	30	30	30
Slit diameter (mm)	2.11	2.39	2.52	3.05	3.26	3.73	4.20
Hole diameter (mm)	1.77	2.12	2.30	2.70	2.87	3.23	3.59
Septa thickness (mm)	0.30	0.30	0.30	0.30	0.30	0.33	0.37
Angular range (degrees)	113	116	120	120	122	122	122
Volumetric sensitivity over whole breast (%)	0.023	0.042	0.065	0.094	0.128	0.164	0.203
Sensitivity in focus (%)	0.101	0.169	0.241	0.346	0.443	0.561	0.687
Optimal iteration	13	17	23	28	28	32	32
Optimal filter FWHM (mm)	4	4	3	2	2	2	1
Optimal TB-CNR	8.4	9.4	8.4	9.0	9.1	7.8	5.1
Standard deviation near chest wall (<5mm)	0.29	0.29	0.31	0.30	0.29	0.29	0.24

5. Conclusion

Results from this paper indicate that fan beam or pinhole collimators might be the best choice for collimation in the studied MBT set-up in terms of TB-CNR while the slit-slat collimators performed significantly worse. Fan beam collimation may have the important advantage that it allows for better imaging near the chest wall.

Acknowledgments

This work is supported by the Dutch Organization for Scientific Research (NWO) under the VIDI grant 12371 'Focused imaging of tumors'.

ORCID iDs

Jarno van Roosmalen https://orcid.org/0000-0001-7043-2587

References

Abreu M C *et al* 2006 Design and evaluation of the clear-PEM scanner for positron emission mammography *IEEE Trans. Nucl. Sci* **53** 71–7
Accorsi R, Novak J R, Ayan A S and Metzler S D 2008 Derivation and validation of a sensitivity formula for slit-slat collimation *IEEE Trans. Med. Imaging* **27** 709–22
Beekman F J 2014 Gamma radiation breast imaging apparatus *Patent: US* 14/044019, NL 2009566
Beekman F J *et al* 2005 U-SPECT-I: a novel system for submillimeter-resolution tomography with radiolabeled molecules in mice *J. Nucl. Med.* **46** 1194–200
Brem R F *et al* 2008 Breast-specific gamma imaging as an adjunct imaging modality for the diagnosis of breast cancer *Radiology* **247** 651–7
Brem R F, Ruda R C, Yang J L, Coffey C M and Rapelyea J A 2016 Breast-specific γ-imaging for the detection of mammographically occult breast cancer in women at increased risk *J. Nucl. Med.* **57** 678–84
Capote R M, Matela N, Conceição R C and Almeida P 2013 Optimization of convergent collimators for pixelated SPECT systems *Med. Phys.* **40** 062501
Cherry S R, Sorenson J A and Phelps M E 2012 *Physics in Nuclear Medicine* (Amsterdam: Elsevier)
Currie L A 1968 Limits for qualitative detection and quantitative determination. Application to radiochemistry *Anal. Chem.* **40** 586–93
Daekwang K and Metzler S D 2012 Finding optimized conditions of slit-slat and multislit-slat collimation for breast imaging *IEEE Trans. Nucl. Sci.* **59** 62–9
Dong S-L *et al* 2011 Development of an adjustable model breast for mammographic dosimetry assessment in Taiwanese women *Am. J. Roentgenol.* **196** W476–81
Formiconi A R 1998 Geometrical response of multihole collimators *Phys. Med. Biol.* **43** 3359
Formiconi A R, Gunter D L, Vanzi E, Martino F D and Volterrani D 2004 *IEEE Nuclear Science Symp. Conf. Record (16–22 October 2004)* (vol 6) pp 3393–7
Fowler A M 2014 A molecular approach to breast imaging *J. Nucl. Med.* **55** 177–80
Gunter D 1996 Collimator characteristics and design *Nucl. Med.* **1** 96–124
Hruska C B 2016 Molecular breast imaging for screening in dense breasts: state of the art and future directions *Am. J. Roentgenol.* **208** 275–83
Hruska C B and O'Connor M K 2008 Quantification of lesion size, depth, and uptake using a dual-head molecular breast imaging system *Med. Phys.* **35** 1365–76
Hruska C B and O'Connor M K 2013 Nuclear imaging of the breast: translating achievements in instrumentation into clinical use *Med. Phys.* **40** 050901
Hruska C B, Weinmann A L and O'Connor M K 2012 Proof of concept for low-dose molecular breast imaging with a dual-head CZT gamma camera. Part I. Evaluation in phantoms *Med. Phys.* **39** 3466–75
Lee T, Braun K, Jaszczak R, Bowsher J and Bobkov K 2004 *Nuclear Science Symp. Conf. Record* vol 5 pp 3352–6

Luo W, Anashkin E and Matthews C G 2010 Performance evaluation of a PEM scanner using the NEMA NU 4-2008 small animal PET standards *IEEE Trans. Nucl. Sci* **57** 94–103
Mankoff D A *et al* 2002 [Tc-99m]-sestamibi uptake and washout in locally advanced breast cancer are correlated with tumor blood flow *Nucl. Med. Biol.* **29** 719–27
Mann S D *et al* 2012 Initial *in vivo* quantification of Tc-99m sestamibi uptake as a function of tissue type in healthy breasts using dedicated breast SPECT-CT *J. Onco.* **2012** 146943
Maublant J *et al* 1996 Technetium-99m-sestamibi uptake in breast tumor and associated lymph nodes *J. Nucl. Med.* **37** 922–5
Mitchell D *et al* 2013 99mTc-sestamibi using a direct conversion molecular breast imaging system to assess tumor response to neoadjuvant chemotherapy in women with locally advanced breast cancer *Clin. Nucl. Med.* **38** 949–56
Moore S C, Kouris K and Cullum I 1992 Collimator design for single photon emission tomography *Eur. J. Nucl. Med.* **19** 138–50
Moyer R 1974 Low-energy multihole converging collimator compared with a pinhole collimator *J. Nucl. Med.* **15** 59–64
Raymond R R *et al* 2008 The positron emission mammography/tomography breast imaging and biopsy system (PEM/PET): design, construction and phantom-based measurements *Phys. Med. Biol.* **53** 637
Rhodes D J *et al* 2015 JOURNAL CLUB: molecular breast imaging at reduced radiation dose for supplemental screening in mammographically dense breasts *Am. J. Roentgenol.* **204** 241–51
Rose A 1973 *Vision: Human and Electronic* (New York: Plenum)
Scopinaro F *et al* 1999 High-resolution scintimammography improves the accuracy of technetium-99m methoxyisobutylisonitrile scintimammography: use of a new dedicated gamma camera *Eur. J. Nucl. Med.* **26** 1279–88
Shepp L A and Vardi Y 1982 Maximum likelihood reconstruction for emission tomography *IEEE Trans. Med. Imag.* **1** 113–22
Shermis R B *et al* 2016 Supplemental breast cancer screening with molecular breast imaging for women with dense breast tissue *Am. J. Roentgenol.* **207** 450–7
Sullivan O, Gong Z, Klanian K, Patel T and Williams M 2012 *Breast Imaging* ed A A Maidment *et al* (Berlin: Springer) pp 300–7
Vaissier P E B *et al* 2012 Fast spiral SPECT with stationary γ-cameras and focusing pinholes *J. Nucl. Med.* **53** 1292–9
van der Have F *et al* 2009 U-SPECT-II: an ultra-high-resolution device for molecular small-animal imaging *J. Nucl. Med.* **50** 599–605
van der Have F, Vastenhouw B, Rentmeester M and Beekman F J 2008 System calibration and statistical image reconstruction for ultra-high resolution stationary pinhole SPECT *IEEE Trans. Med. Imaging* **27** 960–71
van Roosmalen J and Goorden M C 2017 Non-diverging analytical expression for the sensitivity of converging SPECT collimators *Phys. Med. Biol.* **62** N228–43
van Roosmalen J, Beekman F J and Goorden M C 2018 System geometry optimization for molecular breast tomosynthesis with focusing multi-pinhole collimators *Phys. Med. Biol.* **63** 015018
van Roosmalen J, Goorden M C and Beekman F J 2016 Molecular breast tomosynthesis with scanning focus multi-pinhole cameras *Phys. Med. Biol.* **61** 5508–28
Vastenhouw B and Beekman F 2007 Submillimeter total-body murine imaging with U-SPECT-I *J. Nucl. Med.* **48** 487–93
Wang B *et al* 2017 Voxelized ray-tracing simulation dedicated to multi-pinhole molecular breast tomosynthesis *Biomed. Phys. Eng. Express* **3** 045021
Weinmann A L, Hruska C B and O'Connor M K 2009 Design of optimal collimation for dedicated molecular breast imaging systems *Med. Phys.* **36** 845–56